Journal of Industrial and Engineering Chemistry 63 (2018) 426–436

Contents lists available at ScienceDirect

Journal of Industrial and Engineering Chemistry

journal homepage: www.elsevier.com/locate/jiec

Enhancement of the air-stability and optimization of V_{OC} by changing molecular conformation of polyelectrolytes

Min-Hee Choi, Eui Jin Lee, Yong Woon Han, Doo Kyung Moon*

Department of Materials Chemistry and Engineering, Konkuk University, 1 Hwayang-dong, Gwangjin-gu, Seoul 143-701, Korea

ARTICLE INFO

Article history:
Received 10 January 2018
Received in revised form 17 February 2018
Accepted 3 March 2018
Available online 9 March 2018

Keywords:
polyelectrolytes
neutral hole-transporting layer
electronic configuration
molecular geometry
work-function control

ABSTRACT

Three conjugated polyelectrolytes(CPEs) based on thiophene, thieno[3,2-b]thiophene, and 2,2'-bithiophene were designed and synthesized. The CPEs were successfully incorporated into polymer solar cells as pH-neutral hole-transporting layer(HTL) via solution process. The interfacial dipole and work function(WF) of CPE-coated ITO were controlled by the dipole moment of the polymer, which was in turn determined by the stereochemical properties of the molecular structure. CPE-coated ITOs showed sequentially stronger dipole moments due to an increase in the electrostatic repulsion in the molecules. The PCE of device with PFT as the HTL was maintained accompanied by 16% decrease when PEDOT:PSS-based device decreased over 50%.
© 2018 The Korean Society of Industrial and Engineering Chemistry. Published by Elsevier B.V. All rights reserved.

Introduction

In the past decades, polymer solar cells (PSCs) with the bulk heterojunction (BHJ) structure have drawn considerable interest as a promising clean energy source [1–3]. PSCs offer the potential advantages of being lightweight, flexible, and amenable to large-scale production by solution processing. To achieve high-performance PSCs, molecular design of the active materials to optimize the chemical and structural parameters has recently emerged as a major research area [4–6]. Using this approach, power conversion efficiencies (PCEs) of PSCs exceeding 10% have been achieved for single-junction inverted PSCs [7,8]. The rapid development of PCEs has been driven by the development of novel electron-donating and electron-accepting materials. However, the need for enhanced PCE and device stability remains a topical issue [9].

Morphology optimization and interface engineering of BHJ solar cells are also fundamentally important areas of interest. Significant effort has been devoted to the interface engineering of devices, suggesting that the performance and aging of the device are not only dependent on the active layer, but are also governed by the interface with the electrode [10–12]. Interfacial layer materials have played a critical role in enhancing the performance of PSCs. In PSCs, the interfacial layers help form the ohmic contact between the electrodes and active layers, which is of great importance for charge transport and charge collection. At present, developing new interfacial materials has become an effective way to improve the photovoltaic performance of PSCs [13].

In particular, the hole-transporting layer (HTL) between the active layer and conductive indium tin oxide (ITO) electrode of conventional PSCs critically influences the performance and stability of the PSCs [14–16]. Only a few materials have been successfully used as HTLs in PSCs, such as poly(3,4-ethylenedioxy thiophene):(styrenesulfonate) (PEDOT:PSS), MoO_3, WO_3, and V_2O_5 [17,18]. PEDOT:PSS is the most widely employed HTL material for PSCs because of its solution processability, suitable work function (WF), sufficient conductivity, and high optical transparency in the visible–near infrared region. However, PEDOT:PSS is highly acidic and hygroscopic. Furthermore, the strong electrical anisotropy of spin-coated PEDOT:PSS layers, originating from their lamellar structures, often limits charge collection in PSCs [15,16,19,20]. Specifically, this anisotropy determines the chemical instability between the active layer and electrodes in the long term.

It is well known that the stability and large-scale fabrication of PSCs are the two keys to eventual industrialization of PSCs. To meet the demands for industrializing PSCs, conjugated polyelectrolytes (CPEs) are recognized as ideal interfacial materials [21]. CPEs generally consist of three components: the π-conjugated backbone (hydrophobic), the side chains (hydrophobic), and the substituents such as polar/ionic functional groups (hydrophilic). The ionic functional groups are the major components that determine the properties such as the solubility in polar solvents, WF of electrode, and interfacial dipole interactions related to the

* Corresponding author.
E-mail address: dkmoon@konkuk.ac.kr (D.K. Moon).

https://doi.org/10.1016/j.jiec.2018.03.003
1226-086X/© 2018 The Korean Society of Industrial and Engineering Chemistry. Published by Elsevier B.V. All rights reserved.

series resistance, internal built-in voltage, and hole-extraction properties. It is conventionally accepted that the strength, charge selectivity, and direction of the interfacial dipole moment in CPEs are determined by the nature of ionic end-groups. A few researchers like Chen, Bazan, and Lee reported the synthesis of various cationic/anionic CPEs with various polar side chains using an identical backbone [22–24]. When two of these CPEs with identical backbones were applied as the cathode interlayer in PSCs, differences in the interfacial dipole formed by the CPEs arose from differences in the charge, counter-ions, and the pendant groups of them [25]. In the previous studies, the structure–activity relationship between the π-conjugated backbone and the interfacial dipole was not considered. In recent studies, it was reported that the atoms in the side chain or main backbone play a major role in changing the direction and strength of the electric dipole at the interface between the metal electrode and CPE [26,27]. Additionally, variation of the atoms in the side chain or backbone led to broad and stable WF tunability. However, no effective way to modulate the dipole strength was suggested in these studies. Thus, research has been devoted to the development of CPEs by variation of the polymeric structures, including the conjugated backbone [28]. The dipole moments of polymers have long been studied, and the results of experimental studies have demonstrated that the dipole moment of isotactic polymers may be different from that of syndiotactic polymers [29,30] because the conformation of the molecular units should depend on the stereochemical constitution of the chain and should affect the dipole moments of polymer.

In this study, we present the design and synthesis of three alcohol-soluble CPEs based on thiophene, thieno[3,2-b]thiophene, and 2,2'-bithiophene (designated as PFT, PFtT, and PFbT, see Scheme 1). Utilization of the CPEs (by dissolution in methanol) as HTLs instead of PEDOT:PSS is demonstrated. The strength and direction of the dipole moment of the polymer are determined and the effect of the structure of the backbone is analyzed stereochemically. The dipole moment and WF of the CPE-coated anode are controlled based on the number and dihedral angle of the heteroatoms in the polymer backbone. The surface structure of the CPE films is characterized by ultraviolet photoelectron spectroscopy (UPS), atomic force microscopy (AFM) and external electrostatic force microscopy (EFM) analysis. To determine the effects of the structural conformation of CPE, the surface energy, energy level, and hole mobility are investigated. The results demonstrate the importance of selecting a proper π-conjugated monomer with optimal electrical and structural properties for use as the HTL in PSCs. A photo-conversion efficiency (PCE) as high as 7.3% was obtained for the PSCs due to slight improvement of the short-circuit current (J_{sc}) by replacement of PEDOT:PSS with PFT. More importantly, the long-term stability was improved using CPEs as a HTL. Specially, the initial PCE of PFT-based device was maintained accompanied by 16% decrease when PEDOT:PSS-based device decreased over 50%.

Experimental

Materials

All reagents and starting materials were purchased from chemical companies such as Alfa Aesar, Tokyo Chemical Industry (TCI) Co., Ltd., and Sigma Aldrich and used without additional purification. Sodium 4-(2,7-dibromo-9-(4-sulfonatobutyl)-9H-fluoren-9-yl)butyl sulfite (M1) was synthesized by following modified procedures from the literature [24]. Poly({4,8-bis[(2-ethylhexyl)oxy]benzo[1,2-b:4,5-b′]dithiophene-2,6-diyl}{3-fluoro-2-[(2-ethylhexyl)carbonyl]thieno[3,4-b]thiophenediyl}) (PTB7) and 1-(3-methoxycarbonyl)propyl-1-phenyl-[6,6]-C71 ($PC_{71}BM$) were acquired from 1-Material Products and were used as-received. Commercial poly[(9,9-bis(3'-(*N*,*N*-dimethylamino) propyl)-2,7-fluorene)-alt-2,7-(9,9-dioctylfluorene)] (PFN) was also purchased from 1-Material Products and was utilized as the electron transport layer (ETL).

General polymerizations

The monomers, M1 (0.64 g, 1.0 mmol) and M2 (or M3 or M4) (1.0 mmol) (where M2–M4 are stannated thiophene, thieno[3,2-b]

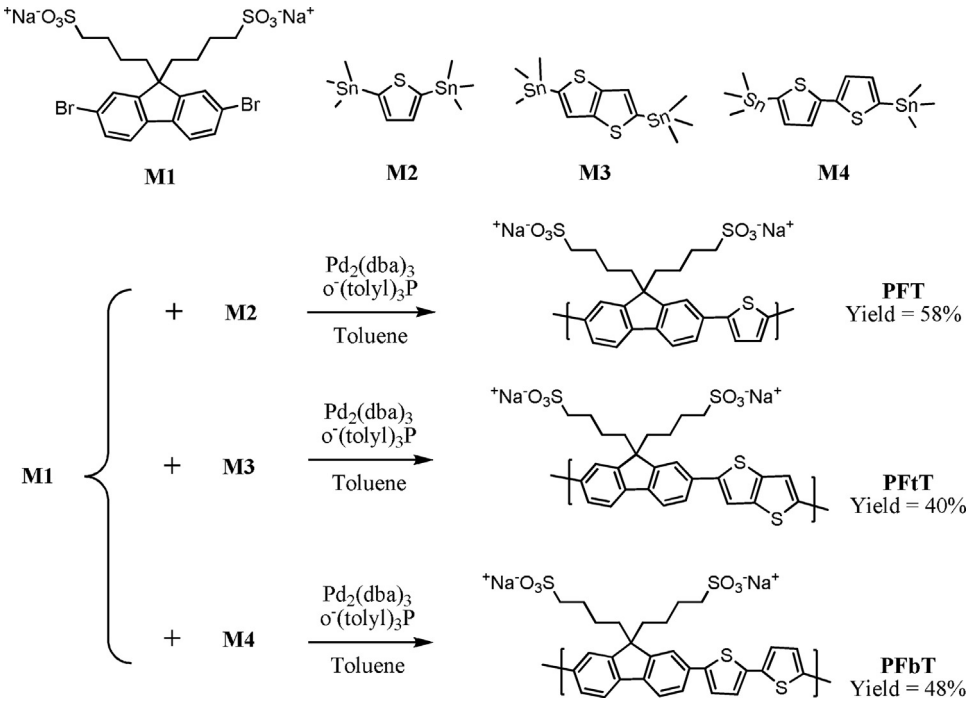

Scheme 1. Synthetic routes of CPE copolymers.

thiophene, and 2,2'-bithiophene, respectively) were dissolved in 27 mL of anhydrous dimethyl formamide (DMF) in a 100 mL flask for flame-drying. The resulting solution was deoxygenated by degassing for 1 h. Tris(dibenzylideneacetone)dipalladium(0) (Pd_2dba_3) (45.8 mg, 0.05 mmol, 5 mol%) and tri-(*o*-tolyl)phosphine (0.06 g, 0.2 mmol, 10 mol%) were added to the stirred solution under a N_2 atmosphere. The reaction mixture was heated and vigorously stirred at 100 °C for 48 h. When polymerization was complete, the viscous mixture was poured into 300 mL of acetone. The precipitate was filtered and washed several times using acetone. The filtered precipitate was further dissolved in water and purified via dialysis using 1 kDa molecular-weight-cut off (MWCO) regenerated cellulose membranes. After dialysis, the water was removed via the low temperature drying method. The alcohol-soluble polymers (PFT, PFtT, and PFbT) were obtained as yellow, brown, and yellowish-green solids, respectively.

Poly[9,9-bis(4′-sulfonatobutyl)fluorene-alt-thiophene] (PFT)

Yellow solid, 0.38 g (yield = 58%). ^{1}H NMR (400 MHz, DMSO-*d*, d): δ 7.85 (d, 2H), 7.68 (s, 2H), 2.35 (m, 2H), 2.14 (s, 3H), 2.08 (s, 2H), 1.56 (m, 2H), 1.42 (m, 4H), 0.56 (m, 2H).

Poly[9,9-bis(4′-sulfonatobutyl)fluorene-alt-thieno[3,2-b]thiophene] (PFtT)

Brown solid, 0.25 g (yield = 40%). ^{1}H NMR (400 MHz, DMSO-*d*, d): δ 7.84 (d, 2H), 7.65 (d, 2H), 7.43 ~ 7.31 (m, 2H), 2.33 (s, 2H), 2.12 (d, 2H), 2.08 (s, 2H), 1.56 (m, 2H), 1.38 (s, 4H), 0.64 ~ 0.52 (m, 2H).

Poly[9,9-bis(4′-sulfonatobutyl)fluorene-alt-2,2′-bithiophene] (PFbT)

Yellowish green solid, 0.31 g (yield = 48%). ^{1}H NMR (400 MHz, DMSO-*d*, d): δ 8.02 (d, 2H), 7.87 (m, 2H), 7.66 (d, 2H), 7.48 ~ 7.26 (m, 1H), 2.41 ~ 2.32 (m, 2H), 2.14 (m, 2H), 2.08 (s, 2H), 1.52 (m, 2H), 1.42 (m, 4H), 0.65 ~ 0.50 (m, 4H).

Measurements

The ^{1}H NMR (400 MHz) spectra were recorded with a Brüker AMX400 spectrometer using D_2O, and the chemical shifts were recorded in units of ppm with tetramethylsilane (TMS) as the internal standard. All gel permeation chromatography (GPC) analyses were carried out using Buffer pH 9 + 30% MeOH as the eluent and PEG/PEO as the calibrant. The thermogravimetric analysis (TGA) was performed using a TG 209 F3 thermogravimetric analyzer. The absorption spectra and transmittance spectra were recorded using an Agilent 8453 UV-visible spectroscopy system. The solutions that were used for the UV-visible spectroscopy measurements were dissolved in MeOH. Theoretical analyses were performed using density functional theory (DFT), as approximated by the B3LYP functional and employing the 6-31G* basis set in Gaussian09. The work function values and UPS profiles of the PFT, PFtT, and PFbT thin films on ITO electrodes were obtained using a UPS analysis chamber (2×10^{-8} Torr) equipped with an AXIS Ultra DLD (KRATOS, Inc.) hemispherical electron energy analyzer with a HeI ($h\nu$ = 21.2 eV) source. The samples were stored under high vacuum overnight before the UPS measurements, and a sample bias of −8.86 V was used for the UPS to determine the WF of the metal. The WF (ϕ_m) is given by: $\phi_m = h\nu - W$, where $h\nu$ is the energy of the incident UV light and W is the measured width of the emitted electrons from the onset of the secondary electrons to the Fermi edge. The current density–voltage (*J*–*V*) data for the photovoltaic devices were acquired using a computer-controlled Keithley 2400 source measurement unit (SMU) equipped with a Class A Oriel solar simulator under AM 1.5G (100 $mW^{\bullet}cm^{-2}$) illumination. The incident photon-to-current conversion efficiency (IPCE) was measured to determine the best device performance using a McScience IPCE measurement system with monochromatic light; the system uses a xenon lamp (Oriel 96000 150 W solar simulator) to pass light through a monochromator (Oriel Cornerstone 130 1/8 m monochromator). The spectral response was normalized by using a standard mono-silicon solar cell before acquiring the IPCE data. Atomic force microscopy (AFM) in tapping mode and electrostatic force microscopy (EFM) analyses were performed using an XE-100 instrument under ambient conditions to obtain topographical images of the HTLs and to determine the surface potentials.

Solar cell fabrication and treatment

All the BHJ solar cells were fabricated with the conventional ITO/HTL/PTB7:$PC_{71}BM$/PFN/Al architecture and were prepared according to the following fabrication procedure from our previous work [31]: ≤10-nm-thick films were prepared by spin-coating MeOH solutions of PFT, PFtT, and PFbT (0.025 ~ 0.25 wt%) on precleaned ITO glass substrates at 3000 rpm for 30 sec in air. For the poly(3,4-ethylene-dioxythiophene):poly(styrene-sulfonate) (PEDOT:PSS, Baytron P 4083 Bayer AG) devices, PEDOT:PSS was passed through a 0.45 mm filter before deposition (at a thickness of ca. 32 nm) on ITO via spin-coating at 4000 rpm in air. These films were also dried at 120 °C for 20 min inside a glove box.

The hole-only devices were fabricated to calculate the hole mobility of the whole devices using the space charge limited current (SCLC) method. The device configuration was as follows: ITO (170 nm)/interlayer/PTB7:$PC_{71}BM$/Ag(100 nm). The mobility can be determined from the slope (≒2) and y-intercept of the log *J*–log *V* graphs of the hole-only devices recorded under dark conditions. The Mott−Gurney equation is as follows [32]:

$$J = \frac{9}{8}\varepsilon\varepsilon_0\mu_{h(e)}\frac{V^2}{L^3}exp\left(0.89\gamma\sqrt{\frac{V}{L}}\right)$$

where *J* is the current density, μ is the zero-field mobility, ε_0 is the vacuum permittivity; ε is the permittivity of the polymer:$PC_{71}BM$ blend, *L* is the thickness of the active layer (80 nm constant); and *V* is the voltage ($V_{bi} - V_r + V_{appl}$), where V_{bi} is the built-in voltage; V_r is the voltage drop because of the series resistance across the electrodes, and V_{appl} is the voltage applied to the device.

Results and Discussion

Synthesis and characterization of polymers

Scheme 1 shows the preparation of a collection of unprecedented *p*-type CPEs via Pd-catalyzed Stille coupling. The resultant

Table 1
Physical and thermal properties of CPEs.

CPE	Yield [%]	Mn[a] [kDa]	Mw[a] [kDa]	PDI[a]	T_d [°C]	UV-vis absorption in MeOH solution λ_{max} [nm]
PFT	58	5.0	11.0	2.18	410	406
PFtT	40	7.7	21.0	2.72	412	430
PFbT	48	8.5	16.9	2.00	418	458

[a] Determined by GPC in Buffer pH 9 + 30% MeOH using PEG/PEO to calibrate.

polymers, i.e., PFT, PFtT, and PFbT, were synthesized with M1 and a π-linker (M2–M4: thiophene, thieno[3,2-b]thiophene, and 2,2'-bithiophene, respectively). The structures of the polymers were confirmed using elemental analysis (EA) and ^{1}H NMR (as shown in the Experimental section and in Fig. S1). These polymers comprised a conjugated backbone with hydrophilic side chains of sodium butane sulfonates (-$C_4H_8SO_3^-Na^+$). PFT, PFtT, and PFbT exhibited excellent solubility in common polar solvents such as ethanol, methanol, 2-methoxyethanol, dimethyl sulfoxide (DMSO), dimethyl formamide (DMF), and water. Upon dissolving the polymers in water/alcohol, the polymers could be incorporated as the HTL in polymer:fullerene BHJ solar cells instead of PEDOT:PSS. The ^{1}H NMR spectra of the three materials showed similar features because of the similarity of the polymer backbones. ^{1}H NMR structural analysis of the obtained polymers showed a peak corresponding to PFbT along with two additional peaks compared with the profile of PFT due to the hydrogens combined with the 3,4-carbon of 2,2'-bithiophene as a π-linker.

Table 1 summarizes the polymerization results and thermal properties of the copolymers. The respective molecular weights (M_w) of PFT, PFtT, and PFbT were 11.0 kDa, 21.0 kDa, and 16.9 kDa, and the corresponding polydispersity indexes (PDIs) were 2.18, 2.72, and 2.00, as determined by GPC using PEG/PEO as a calibrant with Buffer pH 9 + 30% MeOH as the eluent. The thermal stability of the obtained polymers was evaluated using TGA and the resulting profiles are presented in Fig. S2. The TGA profiles of all the

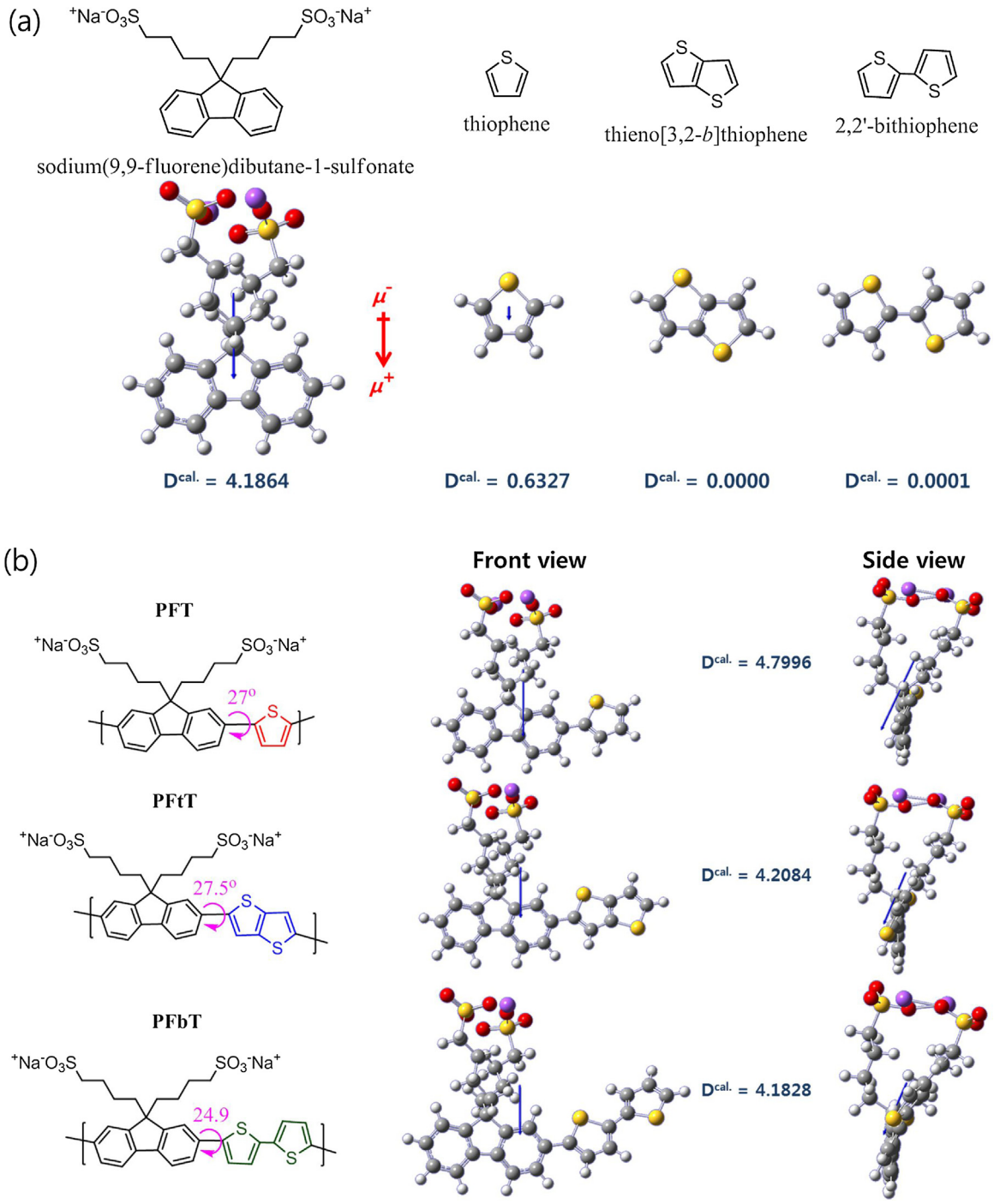

Fig. 1. The calculated results of the geometric structures, dipole moments and direction of monomers (a) and the CPEs (b).

polymers revealed the 'temperature of 5% weight loss' in N_2 environment to be 410 °C or higher. Thus, all of the synthesized CPEs exhibited superior thermal stability, indicative of suitability for device fabrication and application.

Computational study of polymers

Density functional theory (DFT) simulations were performed to identify the molecular geometries, electron density, and dipolar properties of the synthesized polymers. The DFT theoretical calculations were performed with the Gaussian 09 program using the hybrid B3LYP/6-31G(d).

Fig. 1 shows the calculated geometric structures, the dipole moment and its direction of the monomers and the polymers. As shown in Fig. 1(a), each monomer had a different dipole moment. The calculated dipole moments (D^{cal}) for sodium(9,9-fluorene) dibutane-1-sulfonate (F), thiophene (T), thieno[3,2-b]thiophene (tT) and 2,2'-bithiophene (bT) were 4.1864, 0.6327, 0.0000, and 0.0001, respectively. The molecular dipole moment results from non-uniform distribution of the positive and negative charges on the various atoms. The D^{cal}s of the F and T units are ion-induced dipoles (μ_{ID}) generated by electron-enrichment part of the molecular structure, such as by ionic end groups or a nonbonding electron pair. Notably, the F unit had the largest $D^{cal.}$ due to the anionic side chain (-SO_3^-) [33–35]. In a previous study, we presented CPEs having heterocyclic compounds in their backbone [31]. T is an aromatic unsaturated compound having a heteroatom with at least one pair of non-bonding electrons. The heteroatom (herein, sulfur (S)) becomes sp^2-hybridized and develops a negative charge because of its electron pair. This delocalization produces a dipole moment. However, despite having two S atoms in their chemical structures, the D^{cal} values for tT and bT were around zero. Because the two S atoms in tT and bT are symmetrically situated on opposite sides in the optimized structure, there is an offset dipole moment. Therefore, the different π-linkers in the polymers induced differences in the dipoles (4.7996 D in PFT, 4.2084 D in PFtT, and 4.1828 D in PFbT) as shown in Fig. 1(b). Distinguishingly, PFT was composed of monomers with the strongest dipole moment and all the dipoles in the backbone were unidirectionally aligned. Thus, PFT had a much stronger dipole moment than that found in PFtT and PFbT. The dihedral angles of the three polymers between the F unit and the π-linker also were calculated. The dihedral angles of PFT and PFtT (27 and 27.5°) were slightly larger than that of PFbT (24.9°). In contrast with

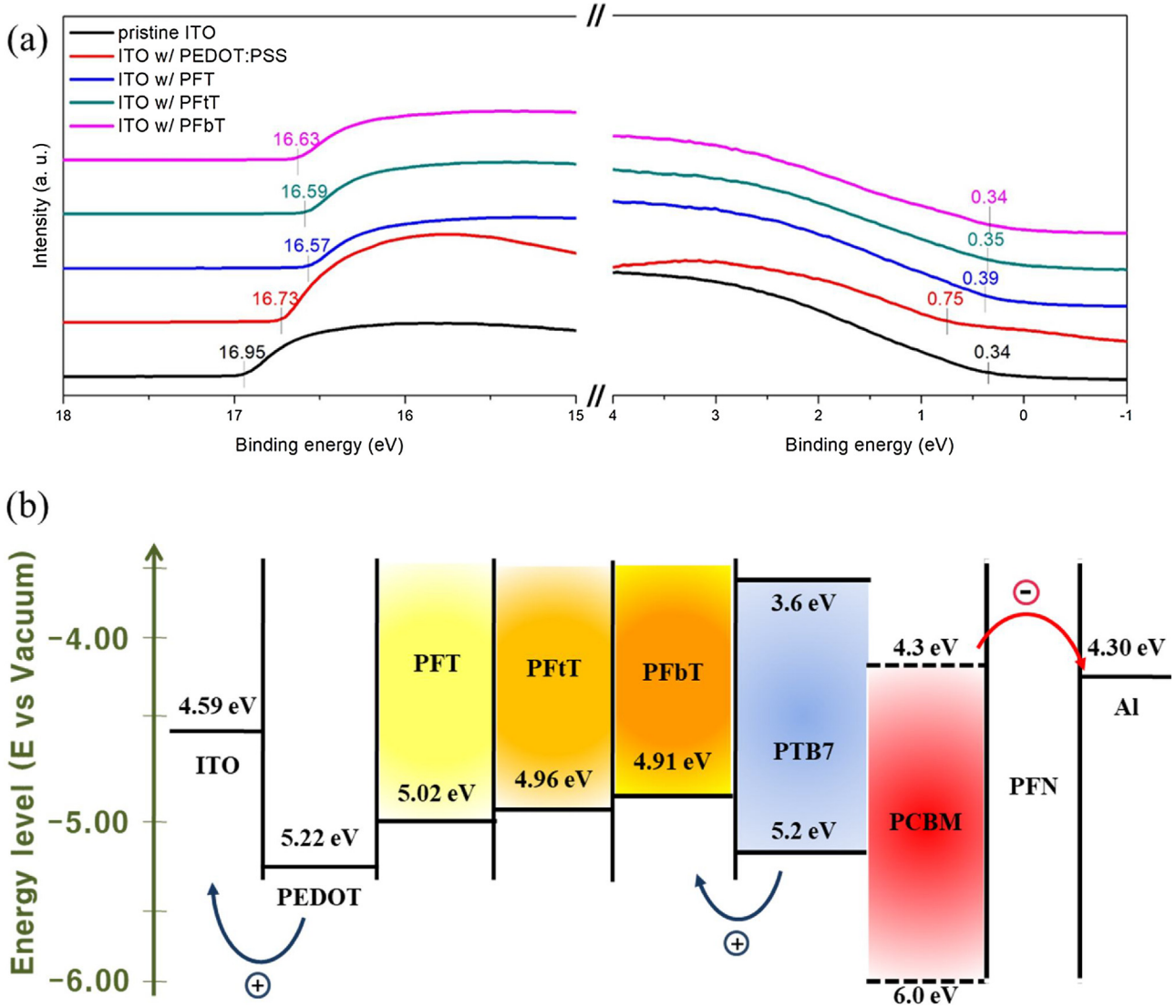

Fig. 2. UPS spectra of the PEDOT:PSS and CPEs (PFT, PFtT and PFbT) coated on top of ITO electrodes. Interfacial energy diagram of the BHJ solar cells with PEDOT:PSS and CPEs as the HTL (b).

the short and rigid π-linkers in PFT and PFtT, the bT-linker makes the backbone of PFbT more flexible and increases the distance between the two polar groups of F, which weakens the repulsion, resulting in a smaller dihedral angle. Due to the decrease of the electrostatic repulsion between the repeating units, the D^{cal} value of PFbT becomes small [36]. The various dipole moments in the polymers have a profound influence on the distribution of the charges, and the structural geometry of the polymers also impacts the dispersion of the electrons [37,38].

Fig. S3 shows the molecular orbitals of the calculated HOMO and LUMO levels of the polymers. The HOMO and LUMO orbitals of PFT, PFtT, and PFbT were delocalized over the polymer main chain; the calculated HOMO levels were −5.60, −5.47, and −5.30 eV, respectively. By increasing the length of the π-linker in the backbone, the HOMO energy level of the polymers tended to increase because the enhancing length of the π-linker led to an increase of the electron-donating ability and conjugation length of the conjugated polymers [39,40]. For the aforementioned reasons, the shallowest HOMO level was obtained for PFbT and the deepest HOMO level was obtained for PFT.

Ultraviolet photoelectron spectroscopy (UPS) analysis

UPS analysis was performed to investigate the effective WF changes in the polymer-covered ITO electrodes with variation of the π-linker and dipole moments. Fig. 2(a) shows the UPS spectra, $E_{cut\text{-}off}$, and E_F of the polymers (PFT, PFtT, and PFbT) coated on ITO. The UPS spectra of pristine ITO glass and PEDOT:PSS-coated ITO are also presented for comparison. The WF values of the polymers were determined by using the equation: $WF = h\nu - (E_{cut\text{-}off} - E_F)$, where $h\nu = 21.2$ eV (the incident photon energy for HeI), $E_{cut\text{-}off}$ occurs at higher binding energy (left), and E_F occurs at lower binding energy (right) [41]. The WF of the bare ITO substrate and PEDOT:PSS coated on ITO were estimated to be 4.59 and 5.22 eV, respectively. WF values of 5.02, 4.96, and 4.91 eV were respectively obtained for PFT, PFtT, and PFbT on top of ITO. Although ultrathin interlayers were spin-coated on the ITO substrate, $E_{cut\text{-}off}$ was obviously down-shifted for the polymer coated-ITOs. $E_{cut\text{-}off}$ corresponds to the vacuum level of the film, which depends on the dipole moment at the interface near the anode. The shift of the vacuum level was equivalent to subtracting the WF of ITO from the difference between the vacuum level of the polymer films and the Fermi energy of ITO [42]. Spontaneous orientation of the ionic group of CPE and its corresponding counter ion generates permanent μ_{ID} dipoles at the ITO/active layer interface, and the formation of interfacial dipoles pointing outwards from ITO may account for the increase of the WF of ITO [22]. Thus, the WF of ITO changed 0.43, 0.40, and 0.32 eV with the introduction of PFT, PFtT, and PFbT, respectively. Based on the UPS data, the energy level diagram of the materials in the PSC devices is illustrated in Fig. 2(b), where the stronger dipole moment of CPE causes the vacuum level and the WF of ITO to be more significantly down-shifted. By coating the CPEs with different π-linkers having sequentially stronger dipole moments (i.e.,bT → tT → T), the secondary cut-off of the CPE-covered ITO electrodes in the range from 16.63 to 16.57 eV was successively shifted to lower binding energies. The WF of the PFT-, PFtT-, and PFbT-coated ITOs assured Ohmic contact. Specially, the WF of the PFT-coated ITO was similar to that of the PEDOT:PSS-coated ITO, the energy levels of which satisfactorily match the HOMO level of the donor material (PTB7). This phenomenon improves the energy alignment and facilitates hole extraction from the donor to the ITO side. Conversely, the WF of the PFtT- and PFbT-coated ITOs was smaller than that of the PEDOT:PSS-coated ITO. Therefore, the energy barrier to hole transport between the ITO anode and the active layer was larger than that of PEDOT:PSS and PFT. For this reason, we predicted that a device using PFtT or PFbT as the HTL should have a lower V_{oc} and J_{sc}. The variation of the WF of the ITO after application of the polymer coating was identical to that predicted from the DFT computations.

We attribute the gradual decrease in the WF of the CPE-covered ITO electrodes to the control provided by the different conjugation lengths and dipole moments of the polymers. CPEs composed of π-conjugated backbones with ionic functional groups can reduce the hole-injection barrier between the metal anodes and organic active layers in thin-film-based electronic devices. This is essential for devices that require energy-level-matching at the interface to achieve high performance. This unique property, referred to as WF tunability, results from the formation of an aligned interfacial dipole assembly at the metal/organic semiconductor interface, which improves charge injection [34].

Optical properties

Fig. 3(a) shows the UV–vis absorption spectra of the PFT, PFtT, and PFbT solutions in methanol. Fig. 3(a) shows the UV–vis absorption spectra of the PFT, PFtT, and PFbT solutions in methanol. As shown in Table 1, the absorption maxima (λ_{max}) of PFT, PFtT, and PFbT at 406, 430, and 458 nm correspond to the π–π* transition from the top of the valence band to the bottom of the conduction band [43]. Compared with the absorption spectra of PFT, the absorption spectra of PFtT and PFbT were red-shifted by 24 and 52 nm in solution, respectively. These extensions in the absorption region are attributable to a reduction in the band-gap due to an

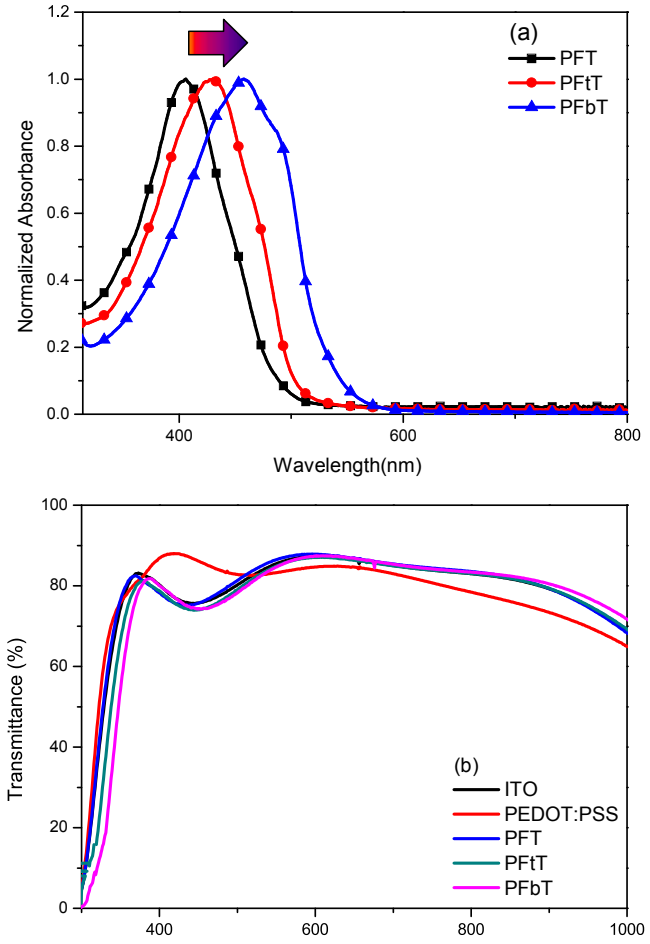

Fig. 3. UV-vis absorption spectra of CPEs (PFT, PFtT and PFbT) in solution (a) and Comparison of transmittance between PEDOT:PSS and polymers on the ITO substrate (b).

increase in the conjugation length of the polymer [39]. The polymers also showed a absorption at 300–600 nm, indicating that these polymers can absorb only in a narrow optical-wavelength range of the solar spectrum and are suitable HTLs because these polymers transfer most of the solar flux to the active layer for energy harvesting.

The transmittance spectra of the PEDOT:PSS and polymer (PFT, PFtT, and PFbT) films spin-coated on ITO substrates are shown in Fig. 3(b). The spectrum of bare ITO is also included for comparison. The transmittance spectra of the polymer films spin-coated on ITO were similar to that of the bare ITO substrate and the polymers showed higher transmittance than PEDOT:PSS in the long-wavelength range (above 534 nm). However, compared with PEDOT:PSS, the PFT, PFtT, and PFbT films exhibited slightly lower optical densities than PEDOT:PSS in the range of 380–534 nm because of the absorption of the polymers [44]. Regardless of the substrates, these polymer films, with a thickness of ~10 nm, exhibited narrow and low light absorption in the visible wavelength region. Therefore, the current density of the PSCs employing PFT, PFtT, and PFbT as the HTL should be higher than that of PEDOT:PSS cells due to the increase of the photon flux of the solar spectrum in the near-IR region.

Contact angles and surface potential energies

As shown in Fig. 4, the contact angles of the polymer(PFT, PFtT, and PFbT)-covered ITO electrodes were 54.8°, 41° and 24.5°, respectively, when measured with deionized water. PFT and PFtT showing a lower wettability on the surface of the PEDOT:PSS-coated and pristine ITO. In addition, the surface energies (45.86 and 56.82 mN/m) were lower in the PFT and PFtT layers than that (60.94 and 70.34 mN/m) of the PEDOT:PSS and pristine ITO layer. This result indicated that the surface characteristic of the ITO changed from hydrophilic to hydrophobic due to the introduction of PFT and PFtT even PEDOT:PSS. Also it indicated that a hydrophobic surface and a photoactive layer could come in close contact when they were stacked, resulting in better wetting by the nonpolar solvents used in the active layer [45].

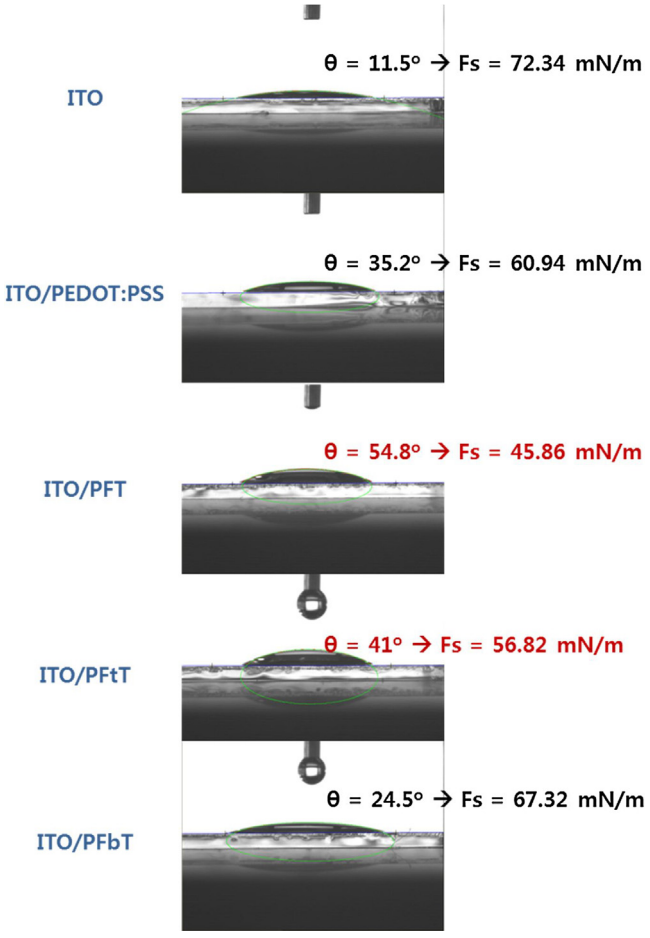

Fig. 4. The contact angle images by dropping DI water on the surface of pristine and polymer-coated ITO.

Based on the comparison of the surface potential values of ITO and polymer-coated ITOs(as seen in Fig. 5), we found that the surface potential of polymer-coated ITOs were smaller than that of ITO. The surface potential is can be affected by electronic states on the surface including surface charge density or surface traps, surface reconstruction, and chemical composition, etc [46]. This indicates a microscopic electric dipole moment with the positive charge end pointing toward the HTL surface and the negative charge end pointing toward the ITO [47]. This result is matched with UPS data that polymer-coated ITOs present deeper work function than the pristine ITO [48]. Moreover, difference in surface potential (ΔSP) of the active layer and anode electrode changed from 84.8 mV to 88.8 mV depending of the type of HTLs. PFbT had the largest ΔSP (88.8 mV), while PFT showed the smallest ΔSP (84.8 mV). As a result, hole transfer was accelerated by the close contact of the two layers and the photovoltaic device performance could be improved, accordingly [9].

Photovoltaic properties

To investigate the influence of the π-linker in the backbones of the CPEs on the device performance, BHJ solar cells were fabricated by using the CPEs as the HTL. The device architecture consisted of ITO/HTL (PFT or PFtT or PFbT or PEDOT:PSS)/PTB7:$PC_{71}BM$/PFN/Al (the device structure is shown in Fig. 6(a)). The active materials were prepared in a solution comprising a blend of PTB7 as the donor and $PC_{71}BM$ as the acceptor (1:1.5 by weight) in a chlorobenzene/1,8-diiodooctane solvent mixture (97:3 by volume). The thickness of active layer was fixed 80 nm which showed best performance [49]. PEDOT:PSS, widely used in solar cells as a HTL, was used as a control for comparative analysis of the performance of the CPEs. The optimal thickness of the CPEs as the HTL was found to be approximately 10 nm for 0.025 wt% methanol solutions at a spin-coating speed of 3000 rpm. Many studies have shown that the use of CPE, which has an ionic side chain, as the HTL in organic electronic devices results in excellent device performance.

As shown in Fig. 6, the polymers have end groups bearing anionic functionalities. By placing the CPEs between the hydrophobic active layer and the hydrophilic ITO anode, the ITO surface is thought to be covered with the $Na^+SO_3^-$ functionalities of the CPEs. The CPEs effectively decreased the WFs of the ITO by introducing ion-induced negative dipoles oriented toward the active layer [33,50]. The present results clearly demonstrate that a large μ_{ID} is generated on the π-conjugated backbone of the CPEs and creates synergy with the interfacial dipole. This explanation is supported by the UPS analysis.

Fig. 7(a) shows the current density–voltage (J–V) curves, demonstrating that the best PSC performance was achieved with PFT or PFtT or PFbT or PEDOT:PSS as the HTL; the data were acquired under AM 1.5 G irradiation (100 $mW^{\bullet}cm^{-2}$). The detailed device parameters are summarized in Table 2.

The highest PCE achieved for the PFT-based device was 7.3%, with a V_{oc} of 0.697 V, a J_{sc} of 15.6 $mA^{\bullet}cm^{-2}$, and a FF of 67.4%. In comparison, for PFtT, the PCE was 6.2%, with a J_{sc} of 15.1 $mA^{\bullet}cm^{2}$, V_{oc} of 0.657 V, and FF of 63.0%. In the case of PFbT, the PCE was 5.3%,

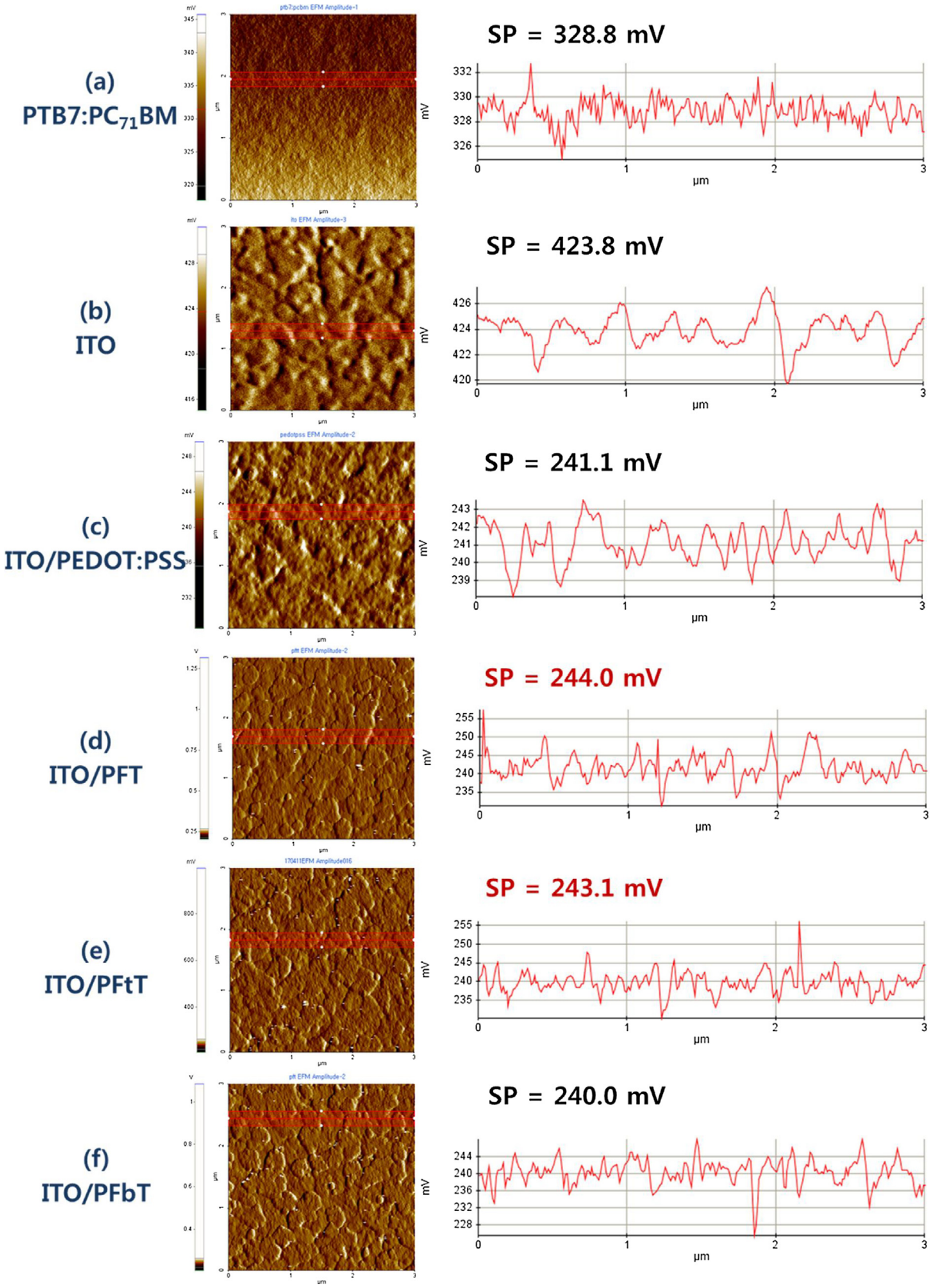

Fig. 5. Surface potential (SP) images and profiles of PTB7:$PC_{71}BM$ (active layer, a), pristine ITO (b) and polymer-coated ITOs: PEDOT:PSS (c), CPE layers (d) ~ (f).

with a J_{sc} of 13.0 mA•cm^2, V_{oc} of 0.556 V, and FF of 64.8%. Replacing PEDOT:PSS with PFtT and PFbT decreased the PCE because of a drop in the $V_{oc,}$ J_{sc} and FF. The decrease in the V_{oc} can be ascribed to a shallower WF for PFtT and PFbT-coated ITO (4.96 and 4.91 eV) than that of PEDOT:PSS (5.22 eV), leading to a larger offset with the HOMO of PTB7 as a donor material. However, the PFT-based device

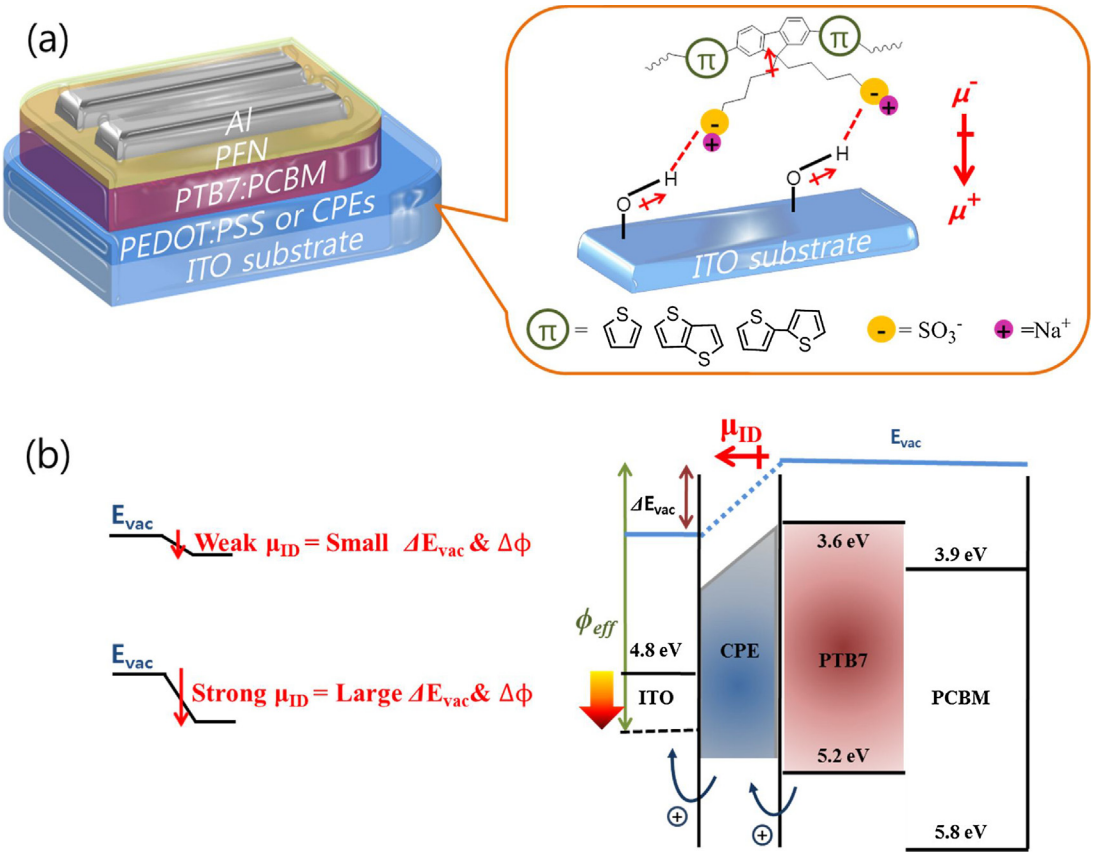

Fig. 6. Schematic illustration of the possible orientations of CPEs on ITO and its' dipole moment (a), proposed CPEs configurations with varying π-derivatives on energy diagram of PSC and their plausible dipole formation (b).

showed same V_{oc} and FF, slight enhancement of the J_{sc} relative to those of the control device employing PEDOT:PSS as the anode interlayer. The PCE of the device employing PFT as the HTL (PCE = 7.3%) reached similar efficiencies of the standard device employing PEDOT:PSS as the HTL (PCE = 7.2%). These results are attributable to the change in the WF of the CPE-covered ITO electrodes. If the CPE has a strong dipole moment in the polymer backbone and at the interface, this leads to larger differences of the voltage in the WF between the ITO/CPE anode and the PFN/Al cathode. For this reason, the V_{oc} increased when the HTL was changed from PFbT to PFT due to the close match with the HOMO energy level of PTB7. This result demonstrates that PFT is an effective material for anode interfacial modification.

The tendency mentioned above is also reflected in the change of the dark curves of the devices (Fig. 7(b)). The device with PEDOT:PSS had a higher current density in forward bias but also a higher leakage current density in reverse bias compared to the of the device with PFT, implying poor diode properties. Thus, the solar cell with PEDOT:PSS as the HTL showed slightly lower J_{sc} than the PFT-based device. This result is consistent with that expected for the CPEs; the diode properties of the CPEs lead to efficient sweep-out of photo-generated charge carriers and hole extraction, and enhanced probability of dissociation of the excitons. Notably, the device fabricated with PFT showed the highest current density in forward bias compared to the devices made with PTtT and PFbT, but the leakage current was low. To understand the effect of the CPEs on the hole transport properties (which influence the current density), hole-only devices comprising the CPEs and PEDOT:PSS interlayers were fabricated with the general device configuration: ITO(170 nm)/HTL/PTB7:PC_{71}BM(80 nm)/Ag(100 nm). The devices were used to test the hole transport properties of the whole devices. The hole mobility of the whole devices with different interlayers was determined from the log J vs. log V graphs presented in the ESI* (Fig. S4 ~ S7, Table S1) via the space charge limited current (SCLC) method. Based on the equation and the log J vs. log V graph, the hole mobility values of the devices employing PEDOT:PSS, PFT, PFtT, and PFbT as the HTL were 4.23×10^{-4}, 3.69×10^{-4}, 3.24×10^{-4} and 3.16×10^{-4} $cm^2 \cdot V^{-1} \cdot s^{-1}$, respectively. The hole mobility of the devices with PEDOT:PSS and CPEs were well matched with photovoltaic properties. These results are consistent with the dark current and leakage current in the dark J–V curves.

Fig. 7(c) shows the IPCE spectra. The external quantum efficiency (EQE) spectra of the same devices were similar to the transmittance spectra of the PFT, PFtT, PFbT, and PEDOT:PSS thin films. The shape of the EQE curve for the devices with these CPEs differed from that of the device with PEDOT:PSS. An increase of the IPCE in the wavelength ranges of 360–458 nm and 542–740 nm was observed for the PFT-based devices. This led to an increase of the J_{sc} from 15.3 mA•cm^{-2} to 15.6 mA•cm^{-2} under integration. The maximum IPCE of the device employing PFT as the HTL exceeded 71.7%, indicative of efficient photon-to-electron conversion.

Interestingly, Fig. 7(d) shows the air stability of devices. The devices employing PFT, PFtT, and PFbT as the HTL without encapsulation were stable over several weeks under ambient conditions. These showed 16, 25.7, and 21.1% decrease of the PCE for over 300 h at room temperature, respectively. This represented an improvement of air stability relative to that of the device with PEDOT:PSS (50.0% decrease of the PCE). It is because of the neutral nature of the CPEs compared with acidic PEDOT:PSS. The PEDOT:PSS thin film is known to cause device degradation in BHJ solar cells due to its acidic and hygroscopic nature [51]; thus, we

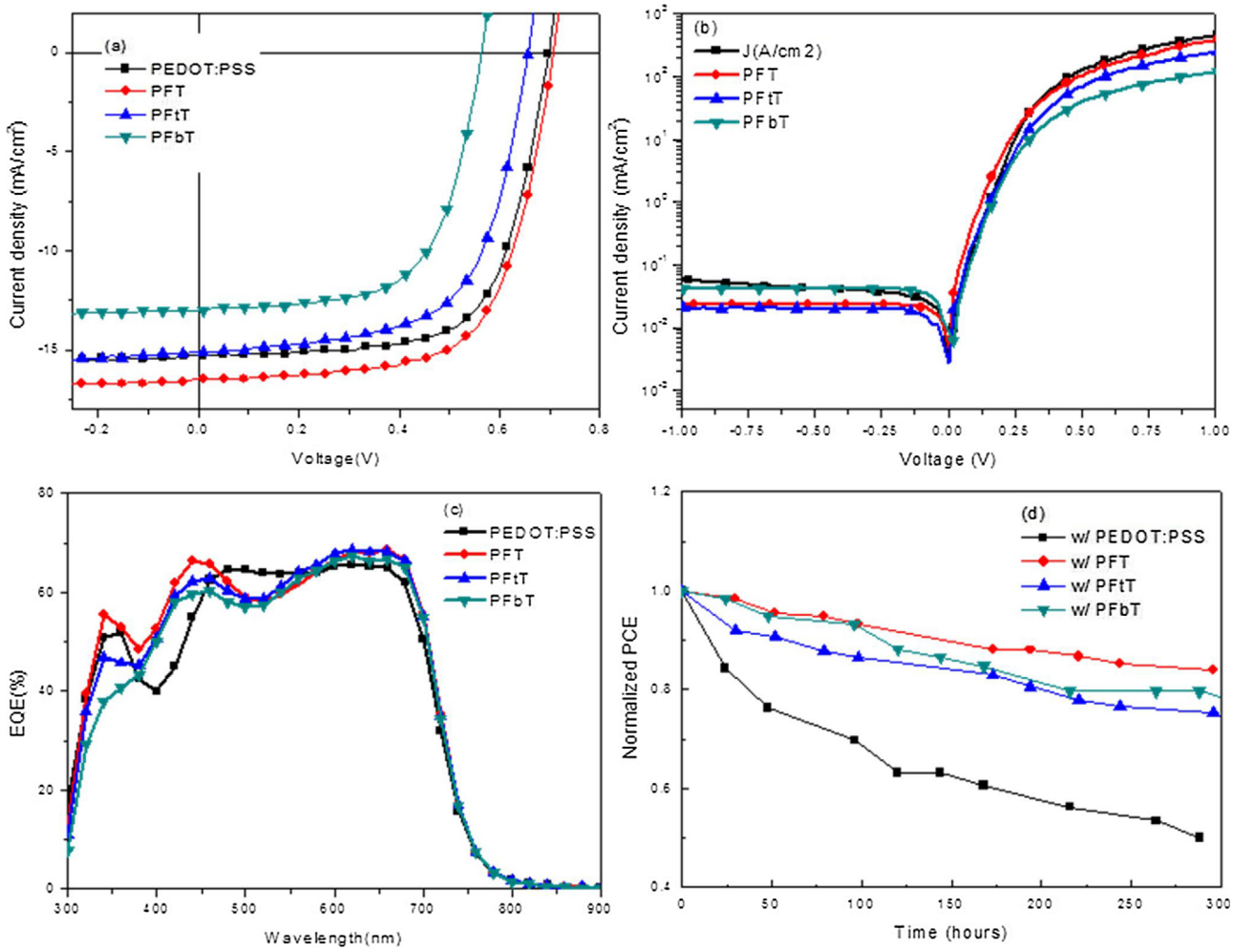

Fig. 7. The J–V curves of the conventional PSC based on PTB7: $PC_{71}BM$ with different HTLs under the illumination of AM 1.5G, 100 mW/cm^2 (a), dark J-V characteristics (b), EQE spectra of the solar cells (c) and air-stability of the solar cells (d).

Table 2
Photovoltaic properties of the BHJ solar cells using PFT, PFtT, PFbT and PEDOT:PSS as HTLs.

CPE	Concentration [wt %]	Jsc [mA/cm^2]	Voc [V]	FF [%]	PCE [%]
PFT	0.025	16.5	0.697	66.4	7.6
PFtT	0.025	15.1	0.657	63.0	6.2
PFbT	0.025	13.0	0.556	64.8	5.3
PEDOT:PSS	–	15.3	0.697	67.3	7.2

attribute the extended lifetime of the PSCs to the neutral pH (6.7–7.0) of the CPE solutions. Notably, longer device lifetimes were obtained with the use of PFT, PFtT, and PFbT. Further, the PFT-based device showed the best performance than that with the others, which indicates that PFT is a promising alternative to PEDOT:PSS as an effective HTL for PSCs.

Morphological analysis

In BHJ solar cells, the surface morphology of the active layer is a critical parameter for determining the efficiency of PSCs. The surface properties of HTLs coated on the ITO anode can significantly affect the morphology of the active layer. AFM was used to investigate the influence of the CPEs (PFT, PFtT, PFbT) and PEDOT:PSS on the surface coverage and morphology of the active layer.

Fig. S8 presents the topographical images of pristine PEDOT:PSS and the CPE layers on ITO. The topographical images of PEDOT:PSS and the CPE surfaces displayed uniform films. Although both PEDOT:PSS and the CPE layers provided uniform films with nanoscale features, the surface roughness of the CPEs was higher, with a root mean square (RMS) roughness of 3.21–3.40 nm, compared with the RMS roughness of PEDOT:PSS (1.56 nm). The corresponding phase images suggest that PEDOT and PSS interconnect with each other without obvious micro-phase separated structures in PEDOT:PSS. However, the CPEs had a granular structure that could be observed. The improved crystallized structure and surface roughness of the CPEs provide strong inter-contact at the interface with the PTB7:$PC_{71}BM$ active layer. Among the CPEs, PFtT exhibited the highest RMS roughness due to the large dihedral angle of the polymer chain compared to that of PFT and PFbT [52,53]. The AFM topographical images of the PTB7:$PC_{71}BM$ BHJ on PEDOT:PSS and the CPEs (Fig. S9) showed that the surfaces were similar to those of the HTLs. The morphologies at the PTB7:$PC_{71}BM$/CPE interfaces were further probed, indicating increased RMS roughness compared with that of the PTB7:$PC_{71}BM$/PEDOT:PSS. In some reports, coarse surface roughness has been attributed to the existence of an interfacial area for charge separation or high crystallinity within two phase networks [9,54]. The high surface roughness along with the high density array of vertical nanopillars facilitated the transport of the holes that were separated from the photoactive layer toward the anode, creating a

large interfacial area between the CPE layer and the photoactive layer. It can be deduced that the CPEs can facilitate hole extraction and also increase the probability of dissociation of excitons into free charge carriers, resulting in improved J_{sc}.

Conclusions

Three alcohol-soluble CPEs, (i.e., PFT, PFtT, and PFbT) were designed and synthesized and were successfully incorporated into organic BHJ solar cells as HTLs via solution processing. The calculated strength and direction of the dipole moment of the polymer confirmed that the D^{cal} of the thiophene derivatives differed according to the tacticity. The stereochemical effect also influenced the CPEs with thiophene derivatives. Based on the UPS data, the dipole moment and WF of the CPE-coated ITO could be controlled. PFT with a single thiophene unit gave rise to a deeper WF than PFtT or PFbT having an atactic thiophene monomer. When BHJ solar cells were fabricated using the CPEs as the HTL, a large μ_{ID} was generated on the CPE possessing a strong D^{cal} with consequent enhancement of the J_{sc} and hole mobility of the devices. Notably, the PFT interlayer provided improved efficiency up to 7.3%, along with improved stability of the PSCs compared with that of the PEDOT:PSS-based device. The drawbacks of the instability of PEDOT:PSS were offset by PFT based on the pH-neutrality and maximized dipole moment of the latter. This study demonstrates the importance of selecting a proper π-conjugated monomer with optimal electrical and structural properties for use as the HTL in PSCs.

Conflict of interest

The authors declare no competing financial interest.

Acknowledgments

This work was supported by “Human Resources Program in Energy Technology” of the Korea Institute of Energy Technology Evaluation and Planning (KETEP), granted financial resource from the Ministry of Trade, industry & Energy, Republic of Korea (No. 20174010201540) and New & Renewable Energy Core Technology Program of the Korea Institute of Energy Technology Evaluation and Planning (KETEP), grant financial resource from the Ministry of Trade, industry & Energy, Republic of Korea (No. 20153010140030).

Appendix A. Supplementary data

Supplementary data associated with this article can be found, in the online version, at https://doi.org/10.1016/j.jiec.2018.03.003.

References

[1] L. Lu, T. Zheng, Q. Wu, A.M. Schneider, D. Zhao, L. Yu, Chemical Reviews 115 (2015) 12666–12731.
[2] I. Etxebarria, J. Ajuria, R. Pacios, Organic Electronics 19 (2015) 34–60.
[3] Y.J. Jeong, J. Jeon, S. Lee, M. Kang, H. Jhon, H.J. Song, C.E. Park, T.K. An, IEEE Journal of the Electron Devices Society 5 (2017) 209–213.
[4] M.-H. Choi, K.W. Song, D.K. Moon, Polymer Chemistry 6 (2015) 2636–2646.
[5] Z. He, C. Zhong, S. Su, M. Xu, H. Wu, Y. Cao, Nature Photonics 6 (2012) 591–595.
[6] L. Ye, S. Zhang, W. Zhao, H. Yao, J. Hou, Chemistry of Materials 26 (2014) 3603–3605.
[7] J.-D. Chen, C. Cui, Y.-Q. Li, L. Zhou, Q.-D. Ou, C. Li, Y. Li, J.-X. Tang, Advanced Materials 27 (2015) 1035–1041.
[8] Y. Liu, J. Zhao, Z. Li, C. Mu, W. Ma, H. Hu, K. Jiang, H. Lin, H. Ade, H. Yan, Nature Communications 5 (2014) 5293.
[9] E.J. Lee, S.W. Heo, Y.W. Han, D.K. Moon, Journal of Materials Chemistry C 4 (2016) 2463–2469.
[10] W.Z. Cai, P. Liu, Y.C. Jin, Q.F. Xue, F. Liu, T.P. Russell, F. Huang, H.L. Yip, Y. Cao, Advanced Science 2 (2015) 1500095.
[11] Z. Wenqing, T. Zhan'ao, Q. Deping, L. Liangjie, X. Qi, L. Shusheng, Z. Hua, L. Yongfang, Journal of Physics D: Applied Physics 45 (2012) 285102.
[12] K. Nakano, K. Tajima, Advanced Materials (2016) n/a-n/a.
[13] B. Xiao, H. Wu, Y. Cao, Materials Today 18 (2015) 385–394.
[14] E.J. Lee, J.P. Han, S.E. Jung, M.H. Choi, D.K. Moon, ACS Applied Materials & Interfaces (2016), doi:http://dx.doi.org/10.1021/acsami.6b09846.
[15] M. Li, W. Ni, B. Kan, X. Wan, L. Zhang, Q. Zhang, G. Long, Y. Zuo, Y. Chen, Physical Chemistry Chemical Physics 15 (2013) 18973–18978.
[16] E. Bovill, N. Scarratt, J. Griffin, H. Yi, A. Iraqi, A.R. Buckley, J.W. Kingsley, D.G. Lidzey, Applied Physics Letters 106 (2015) 073301.
[17] D.-Y. Lee, S.-P. Cho, S.-I. Na, S.-S. Kim, Journal of Industrial and Engineering Chemistry (2016), doi:http://dx.doi.org/10.1016/j.jiec.2016.1009.1010.
[18] J. Meyer, S. Hamwi, M. Kröger, W. Kowalsky, T. Riedl, A. Kahn, Advanced Materials 24 (2012) 5408–5427.
[19] P.F. Ndione, A. Garcia, N.E. Widjonarko, A.K. Sigdel, K.X. Steirer, D.C. Olson, P.A. Parilla, D.S. Ginley, N.R. Armstong, R.E. Richards, E.L. Ratcliff, J.J. Berry, Advanced Energy Materials 3 (2013) 524–531.
[20] J.P. Han, E.J. Lee, Y.W. Han, T.H. Lee, D.K. Moon, Journal of Industrial and Engineering Chemistry 36 (2016) 44–48.
[21] J. Kesters, S. Govaerts, G. Pirotte, J. Drijkoningen, M. Chevrier, N. Van den Brande, X. Liu, M. Fahlman, B. Van Mele, L. Lutsen, D. Vanderzande, J. Manca, S. Clément, E. Von Hauff, W. Maes, ACS Applied Materials & Interfaces 8 (2016) 6309–6314.
[22] L. Chen, C. Xie, Y. Chen, Organic Electronics 14 (2013) 1551–1561.
[23] C.-K. Mai, H. Zhou, Y. Zhang, Z.B. Henson, T.-Q. Nguyen, A.J. Heeger, G.C. Bazan, Angewandte Chemie International Edition 52 (2013) 12874–12878.
[24] B.H. Lee, J.-H. Lee, S.Y. Jeong, S.B. Park, S.H. Lee, K. Lee, Advanced Energy Materials 5 (2015) 1401653.
[25] T.T. Do, H.S. Hong, Y.E. Ha, J. Park, Y.-C. Kang, J.H. Kim, ACS Applied Materials & Interfaces 7 (2015) 3335–3341.
[26] J.-H. Lee, B.H. Lee, S.Y. Jeong, S.B. Park, G. Kim, S.H. Lee, K. Lee, Advanced Energy Materials 5 (2015) 1401653.
[27] X. Liu, R. Xu, C. Duan, F. Huang, Y. Cao, Journal of Materials Chemistry C 4 (2016) 4288–4295.
[28] Y. Cui, B. Xu, B. Yang, H. Yao, S. Li, J. Hou, Macromolecules (2016), doi:http://dx.doi.org/10.1021/acs.macromol.1026b01595.
[29] M. Shima, M. Sato, M. Atsumi, K. Hatada, Polymer Journal 26 (1994) 579–585.
[30] J.A. Hinkley, High Performance Polymers 8 (1996) 427–431.
[31] M.-H. Choi, E.J. Lee, J.P. Han, D.K. Moon, Solar Energy Materials and Solar Cells 155 (2016) 243–252.
[32] P.N. Murgatroyd, Journal of Physics D: Applied Physics 3 (1970) 151.
[33] B.H. Lee, J.-H. Lee, S.Y. Jeong, S.B. Park, S.H. Lee, K. Lee, Advanced Energy Materials 5 (2015) n/a-n/a.
[34] H. Zhou, Y. Zhang, C.-K. Mai, S.D. Collins, T.-Q. Nguyen, G.C. Bazan, A.J. Heeger, Advanced Materials 26 (2014) 780–785.
[35] X. Li, X. Liu, X. Wang, L. Zhao, T. Jiu, J. Fang, Journal of Materials Chemistry 3 (2015) 15024–15029 A.
[36] L. Chen, X. Liu, Y. Wei, F. Wu, Y. Chen, Physical Chemistry Chemical Physics 18 (2016) 2219–2229.
[37] I. Lange, S. Reiter, M. Pätzel, A. Zykov, A. Nefedov, J. Hildebrandt, S. Hecht, S. Kowarik, C. Wöll, G. Heimel, D. Neher, Advanced Functional Materials 24 (2014) 7014–7024.
[38] H.J. Song, E.J. Lee, D.H. Kim, D.K. Moon, S. Lee, Solar Energy Materials and Solar Cells 141 (2015) 232–239.
[39] J. Roncali, Macromolecular Rapid Communications 28 (2007) 1761–1775.
[40] B.-G. Kim, X. Ma, C. Chen, Y. Ie, E.W. Coir, H. Hashemi, Y. Aso, P.F. Green, J. Kieffer, J. Kim, Advanced Functional Materials 23 (2013) 439–445.
[41] H. Zhou, Y. Zhang, C.-K. Mai, J. Seifter, T.-Q. Nguyen, G.C. Bazan, A.J. Heeger, ACS Nano 9 (2015) 371–377.
[42] J.H. Seo, R. Yang, J.Z. Brzezinski, B. Walker, G.C. Bazan, T.-Q. Nguyen, Advanced Materials 21 (2009) 1006–1011.
[43] D.-M. Kim, K.-B. Shim, J.I. Son, S.S. Reddy, Y.-B. Shim, Electrochimica Acta 104 (2013) 322–329.
[44] H. Choi, C.-K. Mai, H.-B. Kim, J. Jeong, S. Song, G.C. Bazan, J.Y. Kim, A.J. Heeger, Nat Commun . 6 (7348) (2015).
[45] T.-H. Lai, S.-W. Tsang, J.R. Manders, S. Chen, F. So, Materials Today 16 (2013) 424–432.
[46] H. Zhou, Y. Zhang, J. Seifter, S.D. Collins, C. Luo, G.C. Bazan, T.-Q. Nguyen, A.J. Heeger, Advanced Materials 25 (2013) 1646–1652.
[47] Z. He, C. Zhong, X. Huang, W.-Y. Wong, H. Wu, L. Chen, S. Su, Y. Cao, Advanced Materials 23 (2011) 4636–4643.
[48] C.T. Howells, K. Marbou, H. Kim, K.J. Lee, B. Heinrich, S.J. Kim, A. Nakao, T. Aoyama, S. Furukawa, J.-H. Kim, E. Kim, F. Mathevet, S. Mery, I.D.W. Samuel, A. Al Ghaferi, M.S. Dahlem, M. Uchiyama, S.Y. Kim, J.W. Wu, J.-C. Ribierre, C. Adachi, D.-W. Kim, P. Andre, Journal of Materials Chemistry 4 (2016) 4252–4263 A.
[49] Z. He, C. Zhong, S. Su, M. Xu, H. Wu, Y. Cao, Nat Photon 6 (2012) 591–595.
[50] J.-H. Lee, B.H. Lee, S.Y. Jeong, S.B. Park, G. Kim, S.H. Lee, K. Lee, Advanced Energy Materials 5 (2015) 1501292.
[51] B. Ecker, J.C. Nolasco, J. Pallarés, L.F. Marsal, J. Posdorfer, J. Parisi, E. von Hauff, Advanced Functional Materials 21 (2011) 2705–2711.
[52] M.-H. Choi, E.J. Ko, Y.W. Han, E.J. Lee, D.K. Moon, Polymer 74 (2015) 205–215.
[53] Y. Yu, Y. Wu, A. Zhang, C. Li, Z. Tang, W. Ma, Y. Wu, W. Li, ACS Applied Materials & Interfaces (2016), doi:http://dx.doi.org/10.1021/acsami.1026b06967.
[54] C.-Y. Li, T.-C. Wen, T.-F. Guo, Journal of Materials Chemistry 18 (2008) 4478–4482.